Fermi surface nesting and topological and magnetoresistance properties of ThX_2 (X = As, Sb, Bi)

Sushree Sarita Sahoo,[1] Ty M. Mason,[2] Stephen B. Dugdale,[2] and V. Kanchana[1,*]
[1]*Department of Physics, Indian Institute of Technology Hyderabad, Kandi 502285, Sangareddy, Telangana, India*
[2]*H. H. Wills Physics Laboratory, University of Bristol, Tyndall Avenue, Bristol BS8 1TL, United Kingdom*

(Received 21 September 2023; revised 10 December 2023; accepted 3 January 2024; published 22 January 2024)

In this constantly expanding and evolving era of advanced technology, there is great demand for a compound that boasts a plethora of exotic properties. To procure such a compound, we conducted a thorough analysis of the lattice and electronic properties of several Th-based compounds using first-principle calculations. A Dirac-like crossing displaying nodal line characteristics has been observed in the phonon spectrum of $ThAs_2$, exhibiting nontriviality that has been further confirmed by a nonzero value of the Berry phase. In the analysis of the electronic structure of all the compounds, we have detected nontrivial topological features that were manifested by means of gap plane and $\mathbb{Z}_2$ calculations. Moreover, a thorough examination of the compounds further revealed the presence of nodal surfaces, which have been analyzed for their intricate symmetry. The Fermi surface of $ThAs_2$ has been scrutinized for nesting properties through the computation of the real and imaginary components of Lindhard susceptibility, which have shown peaks at the same wave vector, indicating the possibility of a charge density wave in this compound. Furthermore, the application of a 5 T magnetic field has revealed a giant negative magnetoresistance in $ThAs_2$ at 10 K. The coexistence of topological fermions and bosons in the same compound is a rare phenomenon and, combined with the probable presence of charge density waves and negative magnetoresistance, this provides an in-depth, comprehensive understanding of its physical properties and also presents a promising platform for further experimental verifications.

DOI: 10.1103/PhysRevB.109.035151

I. INTRODUCTION

In recent years, there has been a substantial surge in scientific interest towards topological materials, prompting extensive theoretical and experimental efforts to explore, predict, and comprehend their fascinating properties. In particular, layered topological materials, with their distinct atomic layering, offer an array of malleable characteristics and promising applications in electronics, optoelectronics, and spintronics. Thus, they have emerged as an exceptionally encouraging category of topological materials, capable of withstanding defects and impurities. The topological characteristics exhibit an exceptional degree of universality, transcending both the gapped states of matter and the states characterized by a specific Fermi surface (FS) contour. Indeed, these properties may endure well into a truly metallic state, featuring an extended FS and a finite density of delocalized states at the chemical potential. The current research interest concerning topological phenomena in condensed matter systems has undergone a partial shift from insulating materials to semimetals and metals. A Weyl semimetal, which is a topological state of matter characterized by linearly dispersing Weyl Fermions in its low-energy bulk electrons, has gained significant attention. The Weyl nodes, characterized by their twofold degeneracy and nonzero chiral charge, are linked along the boundary through Fermi arc surface states. These surface states are anticipated to demonstrate distinctive transport characteristics, including negative magnetoresistance and nonlocal current flow [1–4].

Topological Dirac semimetals (TDSs) are distinguished by the linear contact of bulk bands at distinct points in momentum space. Recently, TDSs have been proposed to exhibit robust Dirac line nodes, which extend the bulk linear contact from discrete points to lines of one dimension. ZrSiS and HfSiS emerged as a family of topological compounds with unique applications due to the presence of Dirac line nodes in the nonsymmorphic crystals safeguarded by nonsymmorphic symmetry [5,6]. HfSiS, a nodal-line semimetal with a large carrier density, establishes the three-dimensional FS consisting of asymmetric water caltroplike electron and barley seedlike hole pockets, displays FS topology, a nontrivial Berry phase, and anisotropic magnetoresistance (MR) [7]. Apart from these, single crystals of $CaMnBi_2$ also exhibit two-dimensional Dirac fermions and quantum MR, with a critical field leading to unsaturated linear MR [8]. The *WHM*-type substances, comprising elements such as W = Zr, Hf, La; H = Si, Ge, Sn, Sb; and M = O, S, Se, and Te, have been anticipated to exhibit topological characteristics. Experimental investigations on ZrGeM, where M denotes S, Se, and Te, have confirmed the existence of topological semimetal states, as per theoretical predictions. These findings have offered significant insights into the modulation of the Dirac state through spin-orbit coupling (SOC) and changes in lattice constants through different combinations of elements in the *WHM* system [9]. Recent advancements in high-resolution electron energy loss spectroscopy have shed light on the presence of topological phonons in graphene, along with topological Dirac points

*kanchana@phy.iith.ac.in

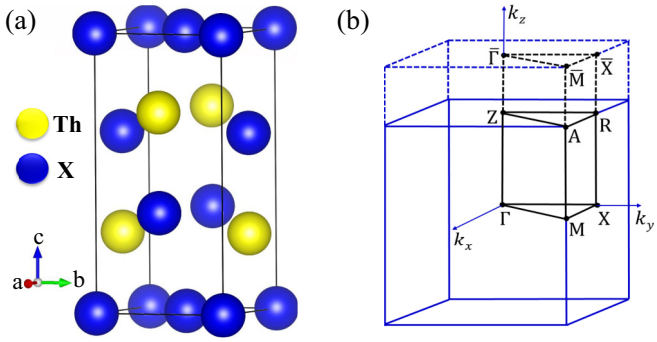

FIG. 1. (a) Crystal structure of ThX_2, (b) The irreducible Brillouin zone illustrating high-symmetry points

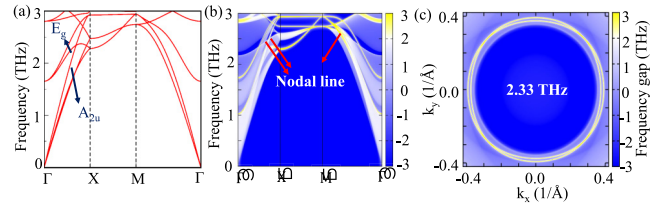

FIG. 3. The (001) plane topological features of phonons $ThAs_2$ in 0–3 THz frequency. (a) Phonon spectra for inverted phonon bands, along with opposite mirror eigenvalues. (b) Bulk crossings in phononic surface states projected in the (001) plane (highlighted with red arrows). (c) The nodal line that corresponds to these bulk band crossings (2.33 THz).

in electrons [10]. It is notable that the discovery of unconventional superconductivity in a graphene superlattice has expanded the scope of exploration in this field [11]. In the case of MgB_2, a high-temperature superconductor, an intriguing inversion, and time-reversal symmetry-protected Dirac nodal line states are revealed in the electronic states [12]. Additionally, MgB_2, with its AlB_2-type centrosymmetric lattice, harbors phononic topological Weyl nodal lines in its bulk phonon spectrum [13]. Transitioning to AV_3Sb_5 compounds (where A is K, Rb, and Cs), the revelation of superconductivity upon cooling has been accompanied by the emergence of intriguing topological features in the electronic structure. FS nesting and charge density wave (CDW) properties further enrich our exploration of these materials [14].

The present paper focuses on an actinide-based series, as these compounds exhibit a plethora of diverse properties, thereby presenting a complex scientific challenge from both a theoretical and practical standpoint, particularly within the nuclear industry. The innovative notions pertaining to the establishment of the thorium fuel cycle as an alternative nuclear energy source have garnered considerable attention due to an abundance of thorium reserves [15,16], thereby generating interest in thorium and its compounds. It is imperative to thoroughly investigate the physical properties that are essential for comprehending the fundamental principles and practical applications of these materials. It is crucial to emphasize that the implementation of compounds in the realm of nuclear industry is contingent upon ongoing research, necessitating thorough testing, qualification, safety assessments, and the development of an efficient radioactive waste management system to ensure adherence to stringent requirements of nuclear safety and reliability, which will take time for widespread deployment. Nevertheless, many thorium-based compounds have previously been investigated for their unique properties. The electronic structure, phonons, electron-phonon coupling, and superconductivity of $ThCoC_2$ have been studied as a function of pressure, with an increase in pressure resulting in an increase in the electron-phonon coupling constant and critical temperature [17]. Another investigation of Th-based compounds compares the electronic structure, mechanical, and dynamical properties, magnetism and electron-phonon coupling of three isostructural superconductors: ThFeAsN, ThCoAsN, and ThNiAsN. The superconducting transition temperature in ThFeAsN is found to be lower than anticipated, although it could be escalated to approximately 10 K owing to the out-of-plane soft phonon modes and reinforcing effects of spin density wave order [18]. In a recent work on $ThIr_2$, the authors studied that the low-frequency phonon modes contribute approximately 24% to the electron-phonon coupling, and the distinct features observed in the low-frequency region of the Eliashberg spectral function are primarily influenced by a significant degree of hybridization between the vibrations of Ir and Th [19].

The preceding discussions and studies on various layered materials, including those based on thorium, have offered compelling motivation to examine materials with extraordinary topological and physical characteristics. In pursuit of this, our investigation has centered on a group of thorium-based PbFCl-like compounds: ThX_2 (with X representing As, Sb, and Bi). Contrary to the experimental synthesis, these materials lack any prior research [20]. The following is the organization of this paper: In Sec. II, details of the

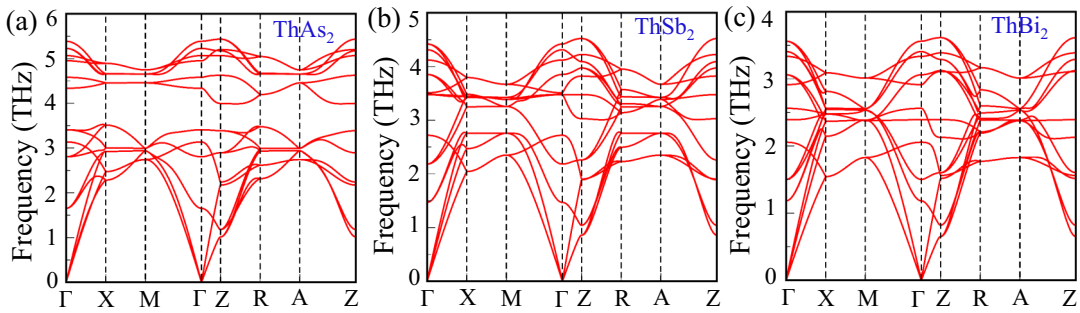

FIG. 2. The calculated phonon spectra of, (a) $ThAs_2$, (b) $ThSb_2$, (c) $ThBi_2$.

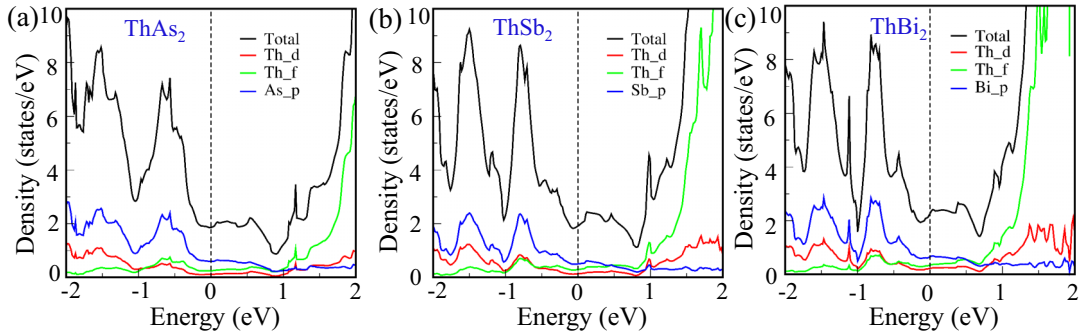

FIG. 4. The DOS, (a) $ThAs_2$, (b) $ThSb_2$, (c) $ThBi_2$.

computation are covered. The specifics of the crystal structure are in Sec. III. The topological characteristics of phonons and electrons are discussed in Secs. IV and V, respectively. The FS properties and MR are covered in Secs. VI and VII and the conclusion is presented in Sec. VIII.

II. COMPUTATIONAL DETAILS

The current investigation employs density functional theory (DFT) through the VASP code for all energy and electronic structure calculations, as detailed in prior works [21,22]. To describe the potential, the projector augmented wave method [23] is employed in conjunction with a plane-wave basis set with a 600 eV energy cutoff for expanding the wave functions. The exchange-correlation functional is determined using the generalized gradient approximation by Perdew *et al.* [24]. The improved tetrahedron method [25] is utilized for the Brillouin zone (BZ) integration over a Γ-centered k mesh. The inclusion of the van der Waals effect is accomplished with the DFT-D3 method [26], given the layered nature of the compound. Electronic structural parameters, such as band structure and FS, are calculated using VASP. The generalized susceptibility, $\chi_0(\mathbf{q}, \omega)$, was computed via eigenvalues and occupancies determined within the full-potential linear augmented plane wave framework, as implemented in the ELK code [27]. The computation of the phonon band spectra is performed by utilizing the combination of the PHONOPY code [28] and the density functional perturbation theory [29] as implemented in VASP. To encompass scattering from the entirety of the phonon band structure, a weighted sum over all Γ-point phonon modes is used to obtain the effective phonon frequency, thereby consolidating it into a single phonon frequency. The combination of VASP2WANNIER90 and WANNIER90 programs [30–33] is used for the study of topological properties. To compute MR, we used the following formula: $\mathrm{MR} = [(\rho_B - \rho_0)/\rho_0] \times 100\%$. Here, ρ_B is resistivity at some finite magnetic field and ρ_0 is resistivity at zero magnetic field. The conductivity tensor that is subject to the magnetic field is calculated by implementing the semiclassical Boltzmann transport theory under the relaxation time approximation [34]. This calculation is performed by utilizing the WANNIERTOOLS package [33].

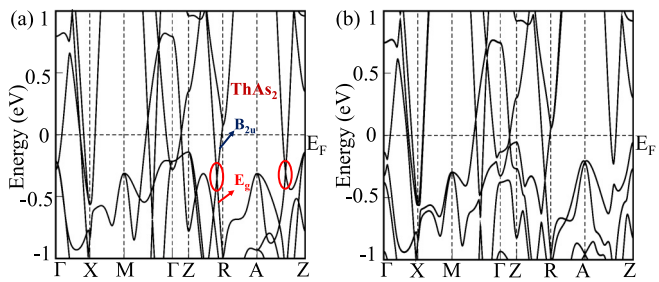

FIG. 5. The band structure of $ThAs_2$ (a) without SOC (b) with SOC.

III. CRYSTAL STRUCTURE

The ThX_2 compound exhibits a tetragonal lattice with a space group of $P4/nmm$ (No. 129), as shown in the Fig. 1, which displays the crystal structure and the irreducible Brillouin zone (IBZ). In this material, the cation atoms (represented by yellow spheres of Th) are staggered above and below square-net atoms (represented by blue spheres of X). The fully relaxed lattice constants of this compound are in good agreement with experimental data [20], as illustrated in Table I. The $P4/nmm$ lattice possesses several notable symmetries, including a fourfold C_{4z} rotation about the z axis, a twofold screw rotation symmetry ($\tilde{C}_{2y}$), and a glide mirror symmetry $\tilde{M}_z$:$(x, y, z) \rightarrow (x + 1/2, y + 1/2, -z)$ with the (001) mirror reflection, followed by a half-translation along the [110] direction, and two mirror reflections with respect to the (100) and $(1\bar{1}0)$ planes, denoted as $M_{(100)}$ and $M_{(1\bar{1}0)}$, respectively. The absence of magnetic ordering preserves time-reversal symmetry ($\mathcal{T}$) in these systems, resulting in a twofold degeneracy of each band at any k point in the BZ. Furthermore, the compound also exhibits inversion symmetry ($\mathcal{I}$), which involves a transformation that replaces each point in the crystal with its mirror image with respect to the center of the unit cell, this being the glide mirror symmetry. Glide

TABLE I. Optimized lattice parameters of ThX_2 (X = As, Sb, Bi) and the experimental parameters.

Compound	$ThAs_2$		$ThSb_2$		$ThBi_2$	
	a(Å)	c(Å)	a(Å)	c(Å)	a(Å)	c(Å)
Experimental [20]	4.086	8.575	4.353	9.172	4.492	9.298
DFT-D3	4.074	8.509	4.373	9.057	4.514	9.233

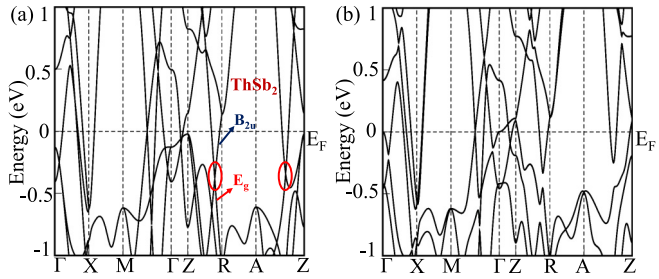

FIG. 6. The band structure of $ThSb_2$ (a) without SOC (b) with SOC.

mirror symmetry is of particular importance for our further discussion.

IV. PHONON TOPOLOGY

To commence, an evaluation of the phonon dispersion was conducted to determine the dynamical stability of the examined compounds. The findings indicated that all phonon modes exhibited positive frequencies, thus affirming their dynamical stability. The phonon dispersion, which is displayed in Fig. 2, was evaluated along the high-symmetry points as shown in the IBZ. As the pnictogen becomes heavier, the phonon modes shift towards the low-frequency region, resulting in greater scattering between optical and acoustic phonon modes. It was also observed that $ThAs_2$ has a finite phonon gap between optical phonon modes located in the highest frequency range, while the other two compounds lacked this feature. This disparity is attributed to the greater difference in the atomic masses of pnictogens present in the compounds. The examination of the $ThAs_2$ phonon dispersion revealed Dirac-like crossings near a phonon frequency of 2.33 THz along paths Γ-*X* and *M*-Γ, which motivated us to investigate the topological nature of these crossings. The analysis of irreducible representation confirmed that the phonon bands had opposite mirror eigenvalues (A_{2u} and E_g), thus ensuring that the nodal crossings were protected against band hybridization. Furthermore, the acoustic-optical phonon mode inversion was verified through an irreducible mode analysis. We utilized the WANNIER90 program to get the tight-binding Hamiltonian for these phonon modes, and subsequently evaluated the surface states and isofrequency spectrum in the 001 plane. The corresponding surface states that displayed bulk and surface state crossings, as well as nodal rings, are depicted in the Fig. 3.

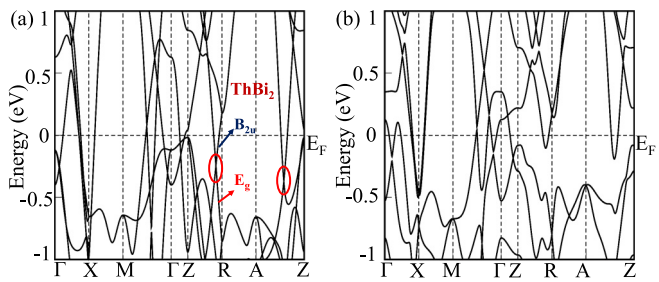

FIG. 7. The band structure of $ThBi_2$ (a) without SOC (b) with SOC.

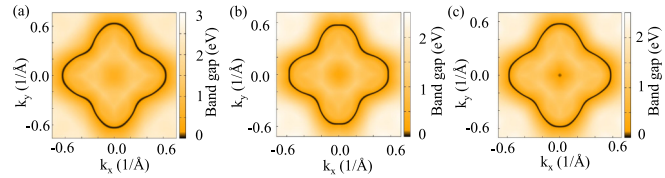

FIG. 8. The isoenergy contours along the *Z*-*R*-*A*-*Z* path, (a) $ThAs_2$, (b) $ThSb_2$, (c) $ThBi_2$.

The glide mirror symmetry, which was mentioned in the previous section, protects the nodal rings. To further substantiate the nontrivial topological character of the phononic states, we computed the Berry phase along a loop in k space comprising a point on the nodal ring. The nonzero Berry phase value confirmed the nontrivial topological nature.

V. ELECTRONIC STRUCTURE AND TOPOLOGY

The dominance of the *p* orbitals of the square-net layer of *X* atoms in the low-energy band structures and the Th-*f* orbitals in the high-energy band structures is evident from the analysis of the density of states (DOS) plot (Fig. 4). Additionally, the Th-*d*, Th-*f*, and *X*-*p* orbitals significantly contribute to the energy bands. The metallic nature of the compounds under investigation is discernible by analyzing the electronic band structure and DOS, which exhibit various bands crossing the Fermi level (Figs. 5–7). In the vicinity of the Fermi level along the *Z*-*R*-*A*-*Z* path, a Dirac-like linearized band dispersion can be observed. We conducted an eigenvalue parity analysis on the bands responsible for the Dirac-like band crossings and discovered that the bands carry opposite mirror eigenvalues, resulting in band inversion in *Z*-*R* path. The presence of multiple Dirac points at different high symmetry points indicating the nodal line is further evidence of the topological features of the investigated compounds. Consequently, the two nontrivial bands, having a constant energy, form a nodal loop below the Fermi level.

To demonstrate the topological features, we conducted energy gap plane calculations corresponding to the band crossings, confirming the occurrence of the nodal line (Fig. 8). The glide mirror symmetry ($\tilde{M}_z$) protects these nodal lines, as evidenced by the symmetry analysis of the $P4/nmm$ crystal structure along these time-reversal invariant momentum (TRIM) points. These compounds, therefore, belong to the topological nodal line metals class, which is a rarely observed phenomenon in materials. The investigation of the compounds has been carried out with the inclusion of SOC. When the cationic atoms are arranged above and below the square net layer with staggered stacking, the degeneracy at the nodal line is eliminated in the presence of SOC [35]. The interaction between the *d* and *f* orbitals of stacking atoms and the *p* orbitals of square-net atoms results in the production of SOC effect.

Upon the inclusion of SOC, a significant gap is observed to open between the crossing points. In $ThBi_2$, the SOC effect is found to be highest, followed by $ThSb_2$ and then $ThAs_2$, which exhibits the least effect due to the low atomic number of As. The examination of the topological properties in the presence of SOC has been carried out by analyzing the $\mathbb{Z}_2$ indices. The results indicate that all three compounds are topologically

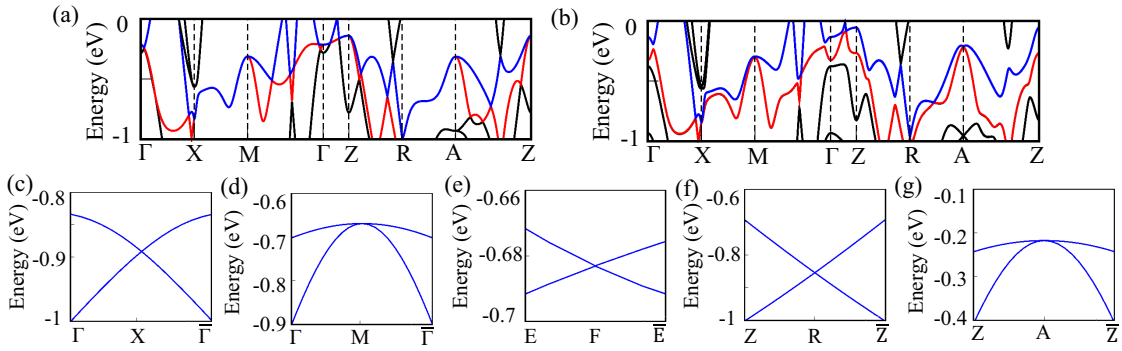

FIG. 9. Electronic band structures near the Fermi level for $ThAs_2$ (a) Band structure without SOC. (b) Band structure with SOC showing the nodal surface. (c)–(g) Continuous crossing along the k path perpendicular to the $k_y = \pm\pi$ plane without SOC. Here, E and F are the midpoints along *X*-*M* and *R*-*A*, respectively.

nontrivial, with the $\mathbb{Z}_2$ indices tabulated below. $ThBi_2$ exhibits a strong topological nature, while $ThAs_2$ and $ThSb_2$ are found to possess a weak topological nature (Table II).

In light of the absence of SOC and the presence of a nodal line, the band crossings along the $k_y = \pm\pi$ plane (along *XM* and *RA* paths) indicate the existence of a 2D nodal surface. This surface is characterized by the fact that each point on it represents a crossing point between two bands whose dispersions are linear along the surface normal direction. The presence of nodal surfaces along the same path was observed in all three compounds, including $ThAs_2$. To gain a deeper understanding of the formation mechanism of nodal surface states in the $k_y = \pm\pi$ plane, we have calculated the band structures along different high-symmetry k paths perpendicular to the $k_y = \pm\pi$ plane, as shown in Fig. 9. It is evident that the band crossing point for every k path is exactly located at the center of the path, which corresponds to a specific nodal point in the $k_y = \pm\pi$ plane. The presence of linear band crossing along the k paths perpendicular to the $k_y = \pm\pi$ plane confirms the twofold band degeneracy between the valence and conduction bands, signifying the nodal surface states in these compounds. The combination of nonsymmorphic space group symmetries, including a glide mirror symmetry ($\tilde{M}_z$), twofold screw rotation symmetry ($\tilde{C}_{2y}$), a mirror M_{xy}, and inversion ($\mathcal{I}$) symmetries, ensures that all bands are degenerate at the *X* and *M* points (*R* and *A* points) in the bulk BZ in the absence of SOC, signifying the presence of twofold band degeneracy between the valance and conduction bands [36]. After the inclusion of SOC, nodal surfaces are generically destroyed as the inversion symmetry remains intact. As $ThAs_2$ exhibits both electron and phonon topology, it was deemed worthy of further investigation.

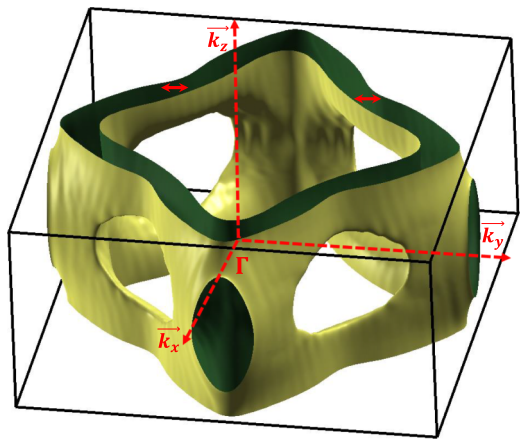

FIG. 10. The calculated Fermi surface of $ThAs_2$ in 3D illustrates a strongly nested sheet, with the proposed nesting vector highlighted with a red double-headed arrow.

VI. FERMI SURFACE

The FS is a fascinating phenomenon that provides a comprehensive overview of the electronic properties [37]. Figure 10 depicts the calculated FS. Upon conducting a visual examination of the 3D FS, it was revealed that there exists a possibility of nesting, as delineated in the diagram. The two FS layers, as depicted in the figure, suggest the likelihood of nesting. It should be noted that relying solely on such an examination may not be adequate for explicitly assessing the nesting characteristics of the FS [38]. To obtain a comprehensive evaluation of the nesting characteristics, we performed the calculation of both the real and imaginary parts of the generalized susceptibility, $\chi_0(\mathbf{q}, \omega)$ (also known as the Lindhard susceptibility), where $\mathbf{q}$ represents the perturbation's wave vector and ω represents its frequency. By ignoring the matrix elements, the noninteracting susceptibility, $\chi_0(\mathbf{q}, \omega)$, for a wave vector $\mathbf{q}$ and frequency ω, can be expressed as shown below:

$$\chi_0(\mathbf{q}, \omega) = \sum_{nn',\mathbf{k}} \frac{f(\epsilon_{n,\mathbf{k}}) - f(\epsilon_{n',\mathbf{k}+q})}{\epsilon_{n,\mathbf{k}} - \epsilon_{n',\mathbf{k}+q} - \omega - i\delta}, \tag{1}$$

where $f(\epsilon)$ denotes the Fermi function and the sum is carried out over bands n and n' throughout the Brillouin zone [39].

TABLE II. Wave function parities calculated along $\mathbb{Z}_2$.

Compound	ν_0	ν_1	ν_2	ν_3	Nature
$ThAs_2$	0	0	0	1	Weak
$ThSb_2$	0	0	0	1	Weak
$ThBi_2$	1	0	0	0	Strong

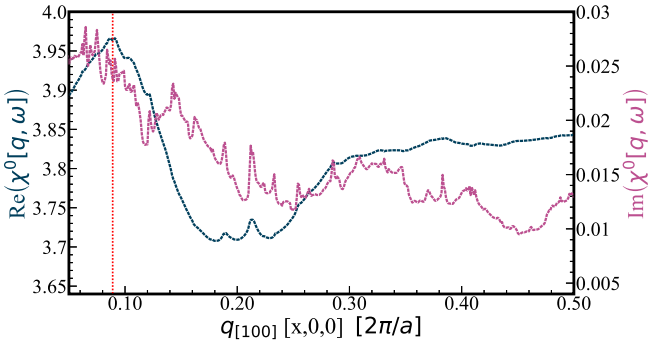

FIG. 11. The calculated generalized susceptibility of $ThAs_2$ along the [100] direction, showing the peak around **q**=0.089a*.The value of ω was chosen to be 3.5 meV, which was the smallest before numerical artifacts are introduced.

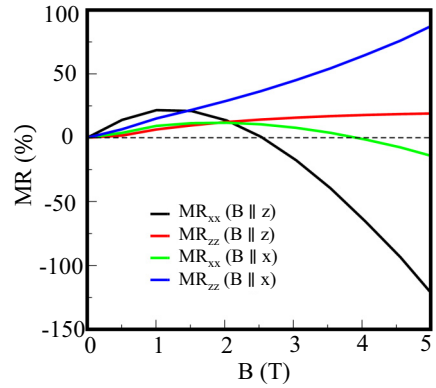

FIG. 12. Magnetoresistance of $ThAs_2$ at 10 K.

While the imaginary component of $\chi_0(\mathbf{q},\omega)$ is exclusively dependent on the details of the electronic structure in the vicinity of the FS and reveals the nesting effects on it, the real part of $\chi_0(\mathbf{q},\omega)$ indicates the electronic response that the electrons will manifest, which may designate, for example, a CDW instability [38].

A genuine nesting effect will be evident through peaks in both the real and imaginary parts at the same wave vector, indicating that the electronic response at a specific frequency stems from the FS geometry. The imaginary and real parts of the noninteracting susceptibility were determined and are presented in Fig. 11. There is a strong peak in the real part of $\chi_0(\mathbf{q},\omega)$ around the **q** vector [0.089, 0.0, 0.0] $\times$ $2\pi/a$ and there are also nesting derived peaks in the imaginary part coming from the nesting of the FS. This peak is due to intraband nesting within the FS sheet shown in Fig. 10, with the nesting vector connecting the two closely separated diamond-shaped surfaces.

The presence of FS nesting in this compound is confirmed by the observed peaks. The nesting of the FS can, under certain circumstances, give rise to a type of electronic instability known as the CDW. This occurs when portions of the FS are parallel and in close proximity, allowing for the creation of a standing wave of charge density. It is important to note that while FS nesting can play a crucial role in CDW formation [40], it is imperative to recognize that this effect alone cannot be considered as the exclusive impetus behind the CDW phenomenon [41]. For this reason, it is crucial to perform additional experimental verifications to corroborate these findings.

VII. MAGNETORESISTANCE

To delve deeper into the physical properties of $ThAs_2$, we have conducted calculations on the MR of this compound, as topological materials are renowned for their extreme MR. The MR was calculated up to an applied field of 5 T at 10 K (Fig. 12), taking into consideration the recent breakthrough of graphene, which demonstrated a large MR of 110% at 300 K and a very low 0.1 T magnetic field, making it particularly suitable for magnetic-sensor and other device applications [42]. To our surprise, the MR values displayed an unusual positive value up to 2.5 T–4 T, but beyond that, it became negative in the x direction and exhibited a giant negative MR (NMR) value. Most materials exhibit positive MR due to the fact that a magnetic field generally restricts a particle's motion. NMR is not prevalent but it has been experimentally verified that certain materials (especially Weyl semimetals) show this type of behavior. Weyl semimetals are one of the most interesting types of materials with NMR, and they belong to a class of topological materials whose most robust properties stem from topology. In contrast to ordinary metals or semiconductors, the MR in Weyl semimetals is highly anisotropic and negative, which is widely considered to be the predominant evidence of the chiral anomaly in transport phenomena. The confirmation of the existence of 3D Weyl points is established through the manifestation of this NMR. As previously discussed, the presence of Dirac points in our electronic structure makes it a nontrivial topological material. The presence of NMR can be ascribed to the transformation of Dirac points to Weyl points induced by the the application of a magnetic field, as mentioned in previous literature [43]. Gorbar *et al.* noted that relaxing the inversion or time-reversal symmetry condition eliminates the degeneracy in the dispersion relations of the left- and right-hand Weyl modes. Consequently, this leads to the conversion of Dirac semimetals into Weyl semimetals. Disrupting time-reversal symmetry with a magnetic field allows for the engineering of a Weyl semimetal from a Dirac semimetal through the application of an external magnetic field. Similar mechanisms have been documented in Na_3Bi and Cd_3As_2 [44].

The Weyl metallic phase is distinguished by a distinctive characteristic in which the transference of a Weyl fermion state from one Weyl point to another occurs through the driving of currents along the momentum direction to link the two paired Weyl points. This occurrence is widely known as the Adler-Bell-Jackiw anomaly, indicating the nonconservation of the chiral current. A previous investigation provided evidence that this atypical longitudinal magnetic resonance stems from the inhibition of scattering between two Weyl points when magnetic fields are augmented [45]. It can be speculated that the negative value of MR exhibits a strong feature of chiral anomaly in the investigated material upon application of a magnetic field, which is further enhanced with an increase in field intensity. It has been previously reported in Na_3Bi that

the chiral anomaly leads to a transfer of charge between Weyl nodes of opposite chirality, resulting in a finite longitudinal conductivity even in the absence of an external electric field [46]. Other Dirac materials such as $YCuAs_2$ [47], Cr doped topological insulators [48], Weyl semimetal TaAs [49], and MPn_2 (M = Nb and Ta; Pn = As and Sb) [50] have also reported NMR. Nevertheless, the precise cause of the origin of NMR in these compounds continues to rely on experimental validation due to the scarcity of theoretical calculations regarding MR and the absence of any convincingly satisfactory explanation for the genesis of NMR.

VIII. CONCLUSION

In brief, our paper has focused on the examination of the electronic and lattice structures of ThX_2 compounds. Our investigation of these compounds has revealed that $ThAs_2$ possesses noteworthy topological properties in its phonon spectrum, which were initially anticipated due to the existence of a Dirac-like crossing at low frequencies. Further analysis validated the existence of a nodal line and a nonzero Berry phase, thereby confirming its nontrivial nature. As for the electronic aspect, all three compounds displayed topological features which were verified by the bulk gap plane and $\mathbb{Z}_2$ calculations. Additionally, nodal surfaces have been observed in all compounds, and their detailed symmetry analysis has also been carried out. The coexistence of electron and phonon topology in $ThAs_2$ prompted us to conduct further investigations. Upon examining the FS of this compound, we detected a high degree of nesting, implying the possibility of a CDW feature. This is supported by the calculation of Lindhard susceptibility, which shows a peak in the real part at the same wave vector as a peak in the imaginary part, making this compound a rare find indeed. To explore more on the physical properties of this compound, we conducted MR calculations up to an applied field of 5 T at 10 K and demonstrated a giant NMR value. Although the origin of the CDW and its intricate interplay with the topological state remain to be determined, our findings point towards the potential presence of a superconducting nature in these topological materials, which presents an exciting avenue for future exploration.

ACKNOWLEDGMENTS

Both S.S.S. and V.K. acknowledge the CSIR project with Sanction No. 03(1433)/18/EMR-II for financial support and IIT Hyderabad for providing computational facilities. The authors also thank the National Supercomputing Mission (NSM) for providing computing resources of PARAM SEVA at IIT, Hyderabad, which is implemented by C-DAC and supported by the Government of India's Ministries of Electronics and Information Technology (MeitY) and Department of Science and Technology (DST). The authors express their gratitude for Projects No. CRG/2022/005228 and DST-FIST No. SR/FST/PSI-215/2016 for their financial assistance. S.B.D. and T.M.M. acknowledge the Advanced Computing Research Centre, University of Bristol [51].

[1] P. Hosur, Friedel oscillations due to Fermi arcs in Weyl semimetals, Phys. Rev. B **86**, 195102 (2012).
[2] D. T. Son and B. Z. Spivak, Chiral anomaly and classical negative magnetoresistance of Weyl metals, Phys. Rev. B **88**, 104412 (2013).
[3] M. M. Vazifeh and M. Franz, Electromagnetic response of Weyl semimetals, Phys. Rev. Lett. **111**, 027201 (2013).
[4] T. Ojanen, Helical Fermi arcs and surface states in time-reversal invariant Weyl semimetals, Phys. Rev. B **87**, 245112 (2013).
[5] C. Chen, X. Xu, J. Jiang, S. C. Wu, Y. P. Qi, L. X. Yang, M. X. Wang, Y. Sun, N. B. M. Schröter, H. F. Yang, L. M. Schoop *et al.*, Dirac line nodes and effect of spin-orbit coupling in the nonsymmorphic critical semimetals MSiS (M = Hf, Zr), Phys. Rev. B **95**, 125126 (2017).
[6] L. M. Schoop, M. N. Ali, C. Straßer, A. Topp, A. Varykhalov, D. Marchenko, V. Duppel, S. S. Parkin, B. V. Lotsch, and C. R. Ast, Dirac cone protected by non-symmorphic symmetry and three-dimensional Dirac line node in ZrSiS, Nat. Commun. **7**, 11696 (2016).
[7] N. Kumar, K. Manna, Y. Qi, S. C. Wu, L. Wang, B. Yan, C. Felser, and C. Shekhar, Unusual magnetotransport from Si-square nets in topological semimetal HfSiS, Phys. Rev. B **95**, 121109(R) (2017).
[8] K. Wang, D. Graf, L. Wang, H. Lei, S. W. Tozer, and C. Petrovic, Two-dimensional Dirac fermions and quantum magnetoresistance in $CaMnBi_2$, Phys. Rev. B **85**, 041101(R) (2012).
[9] J. Hu, Y. L. Zhu, D. Graf, Z. J. Tang, J. Y. Liu, and Z. Q. Mao, Quantum oscillation studies of the topological semimetal candidate ZrGeM (M = S, Se, Te), Phys. Rev. B **95**, 205134 (2017).
[10] J. Li, J. Li, J. Tang, Z. Tao, S. Xue, J. Liu, H. Peng, X.-Q. Chen, J. Guo, and X. Zhu, Direct observation of topological phonons in graphene, Phys. Rev. Lett. **131**, 116602 (2023).
[11] Y. Cao, V. Fatemi, S. Fang *et al.*, Unconventional superconductivity in magic-angle graphene superlattices, Nature (London) **556**, 43 (2018).
[12] K. H. Jin, H. Huang, J. W. Mei *et al.*, Topological superconducting phase in high-T_c superconductor MgB_2 with Dirac-nodal-line fermions, npj Comput Mater **5**, 57 (2019).
[13] J. Li, Q. Xie, J. Liu, R. Li, M. Liu, L. Wang, D. Li, Y. Li, and X.-Q. Chen, Phononic Weyl nodal straight lines in MgB_2, Phys. Rev. B **101**, 024301 (2020).
[14] F. Kaboudvand, S. M. L. Teicher, S. D. Wilson, R. Seshadri, and M. D. Johannes, Fermi surface nesting and the Lindhard response function in the kagome superconductor CsV_3Sb_5, Appl. Phys. Lett. **120**, 111901 (2022).
[15] U. E. Humphrey, M. U. Khandaker, Viability of thorium-based nuclear fuel cycle for the next generation nuclear reactor: Issues and prospects, Renewable Sustainable Energy Rev. **97**, 259 (2018).
[16] C. J. Rhodes, Current Commentary: Thorium-based nuclear power, Science Prog. **96**, 200 (2013).
[17] G. Kuderowicz, P. Wójcik, and B. Wiendlocha, Pressure effects on the electronic structure, phonons, and superconductivity of noncentrosymmetric $ThCoC_2$, Phys. Rev. B **105**, 214528 (2022).

[18] S. Sen and G. Y. Guo, Electronic structure, lattice dynamics, and magnetic properties of ThXAsN (X = Fe, Co, Ni) superconductors: A first-principles study, Phys. Rev. B **102**, 224505 (2020).

[19] H. Y. Uzunok, H. M. Tütüncü, S. Bağcı, The effect of spin-orbit coupling on the physical and superconducting properties of the Ir-rich cubic Laves superconductors AIr_2 (A= Y, Lu, and Th), J. Phys. Chem. Solids **174**, 111178 (2023).

[20] F. Hulliger, New ternary thorium and uranium compounds MYX, J. Less-Common Met. **16**, 113 (1968).

[21] G. Kresse and J. Furthmüller, Efficient iterative schemes for ab initio total-energy calculations using a plane-wave basis set, Phys. Rev. B **54**, 11169 (1996).

[22] G. Kresse and D. Joubert, From ultrasoft pseudopotentials to the projector augmented-wave method, Phys. Rev. B **59**, 1758 (1999).

[23] P. E. Blöchl, Projector augmented-wave method, Phys. Rev. B **50**, 17953 (1994).

[24] J. P. Perdew, K. Burke, and M. Ernzerhof, Generalized gradient approximation made simple, Phys. Rev. Lett. **77**, 3865 (1996).

[25] P. E. Blöchl, O. Jepsen, and O. K. Andersen, Improved tetrahedron method for Brillouin-zone integrations, Phys. Rev. B **49**, 16223 (1994).

[26] S. Grimme, J. Antony, S. Ehrlich, and H. Krieg, A consistent and accurate ab initio parametrization of density functional dispersion correction (DFT-D) for the 94 elements H-Pu, J. Chem. Phys. **132**, 154104 (2010).

[27] J. K. Dewhurst, S. Sharma, and C. Ambrosch-Draxl, ELK FP-LAPW Code, http://elk.sourceforge.net (2013).

[28] T. Atsushi and T. Isao, First principles phonon calculations in materials science, Scr. Mater. **108**, 15 (2015).

[29] G. Xavier and L. Changyol, Dynamical matrices, Born effective charges, dielectric permittivity tensors, and interatomic force constants from density-functional perturbation theory, Phys. Rev. B **55**, 10355 (1997).

[30] N. Marzari and D. Vanderbilt, Maximally localized generalized Wannier functions for composite energy bands, Phys. Rev. B **56**, 12847 (1997).

[31] A. A. Mosto, J. R. Yates, G. Pizzi, Y. S. Lee, I. Souza, D. Vanderbilt, and N. Marzari, An updated version of Wannier90: A tool for obtaining maximally-localised Wannier functions, Comput. Phys. Commun. **185**, 2309 (2014).

[32] M. P. L. Sancho, J. M. L. Sancho, J. M. L. Sancho, and J. Rubio, Highly convergent schemes for the calculation of bulk and surface green functions, J. Phys. F **15**, 851 (1985).

[33] Q. Wu, S. Zhang, H.-F. Song, M. Troyer, and A. A. Soluyanov, WannierTools: An open source software package for novel topological materials, Comput. Phys. Commun. **224**, 405 (2018).

[34] G. K. Madsen and D. J. Singh, Boltztrap. A code for calculating band-structure dependent quantities, Comput. Phys. Commun. **175**, 67 (2006).

[35] I. Lee, S. I. Hyun, J. H. Shim, Topological classification of nodal-line semimetals in square-net materials, Phys. Rev. B **103**, 165106 (2021).

[36] W. Wu, Y. Liu, S. Li, C. Zhong, Z. M. Yu, X. L. Sheng, Y. X. Zhao, and S. A. Yang, Nodal surface semimetals: Theory and material realization, Phys. Rev. B **97**, 115125 (2018).

[37] S. B. Dugdale, Life on the edge: A beginner's guide to the Fermi surface, Phys. Scr. **91**, 053009 (2016).

[38] M. D. Johannes and I. I. Mazin, Fermi surface nesting and the origin of charge density waves in metals, Phys. Rev. B **77**, 165135 (2008).

[39] J. Laverock, T. D. Haynes, C. Utfeld, and S. B. Dugdale, Electronic structure of RNiC_2 (R = Sm, Gd, and Nd) intermetallic compounds, Phys. Rev. B **80**, 125111 (2009).

[40] K. Y. Shin, J. Laverock, Y. Q. Wu, C. L. Condron, M. F. Toney, S. B. Dugdale, M. J. Kramer, and I. R. Fisher, Charge density wave formation in R_2Te_5 (R = Nd, Sm, and Gd), Phys. Rev. B **77**, 165101 (2008).

[41] M. D. Johannes, I. I. Mazin, and C. A. Howells, Fermi-surface nesting and the origin of the charge-density wave in $NbSe_2$, Phys. Rev. B **73**, 205102 (2006).

[42] N. Xin, J. Lourembam, P. Kumaravadivel, A. E. Kazantsev, Z. Wu, C. Mullan, J. Barrier, A. A. Geim, I. V. Grigorieva, A. Mishchenko, A. Principi, Giant magnetoresistance of Dirac plasma in high-mobility graphene, Nature (London) **616**, 270 (2023).

[43] J. Cano, B. Bradlyn, Z. Wang, M. Hirschberger, N. P. Ong, and B. A. Bernevig, Chiral anomaly factory: Creating Weyl fermions with a magnetic field, Phys. Rev. B **95**, 161306(R) (2017).

[44] E. V. Gorbar, V. A. Miransky, and I. A. Shovkovy, Chiral anomaly, dimensional reduction, and magnetoresistivity of Weyl and Dirac semimetals, Phys. Rev. B **89**, 085126 (2014).

[45] H. J. Kim, K. S. Kim, J. F. Wang, M. Sasaki, N. Satoh, A. Ohnishi, M. Kitaura, M. Yang, and L. Li, Dirac versus Weyl fermions in topological insulators: Adler-Bell-Jackiw anomaly in transport phenomena, Phys. Rev. Lett. **111**, 246603 (2013).

[46] J. Xiong, S. K. Kushwaha, T. Liang, J. W. Krizan, M. Hirschberger, W. Wang, R. J. Cava, and N. P. Ong, Evidence for the chiral anomaly in the Dirac semimetal Na_3Bi, Science **350**, 413 (2015).

[47] B. Kang, Z. Liu, D. Zhao, L. Zheng, Z. Sun, J. Li, Z. Wang, T. Wu, and X. Chen, Giant negative magnetoresistance beyond chiral anomaly in topological material $YCuAs_2$, Adv. Mater. **34**, 2201597 (2022).

[48] Q. Guo, Y. Wu, D. Wang, G. Han, X. Wang, L. Fu, L. Wang, W. He, T. Zhu, Z. Zhu, T. Liu, Enhanced negative magnetoresistance near the charge neutral point in Cr doped topological insulator, RSC Adv. **11**, 13964 (2021).

[49] X. Huang, L. Zhao, Y. Long, P. Wang, D. Chen, Z. Yang, H. Liang, M. Xue, H. Weng, Z. Fang, and X. Dai, Observation of the chiral-anomaly-induced negative magnetoresistance in 3D Weyl semimetal TaAs, Phys. Rev. X **5**, 031023 (2015).

[50] Y. Li, Z. Wang, Y. Lu, X. Yang, Z. Shen, F. Sheng, C. Feng, Y. Zheng, and Z. A. Xu, Negative magnetoresistance in topological semimetals of transition-metal dipnictides with nontrivial $\mathbb{Z}_2$ indices, arXiv:1603.04056.

[51] http://bris.ac.uk/acrc.